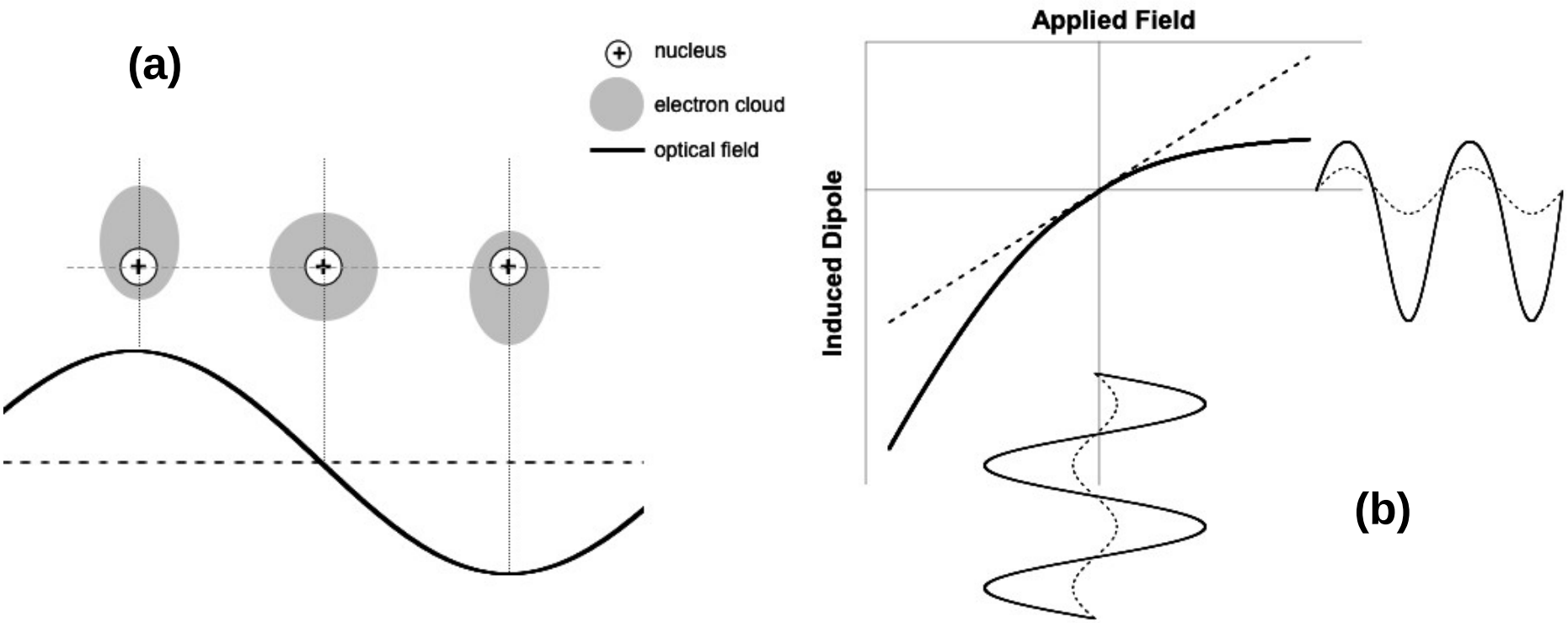

Figure 17.1 (a) Depicts the oscillatory motion of the electron charge cloud about its nucleus in the presence of an applied electric field. (b) Plot of the motion of the induced dipole versus applied electric field. For small magnitude fields the dipole motion responds linearly to the applied field (dashed lines); for large magnitude fields the motion becomes nonlinear with respect to the field strength (solid lines).

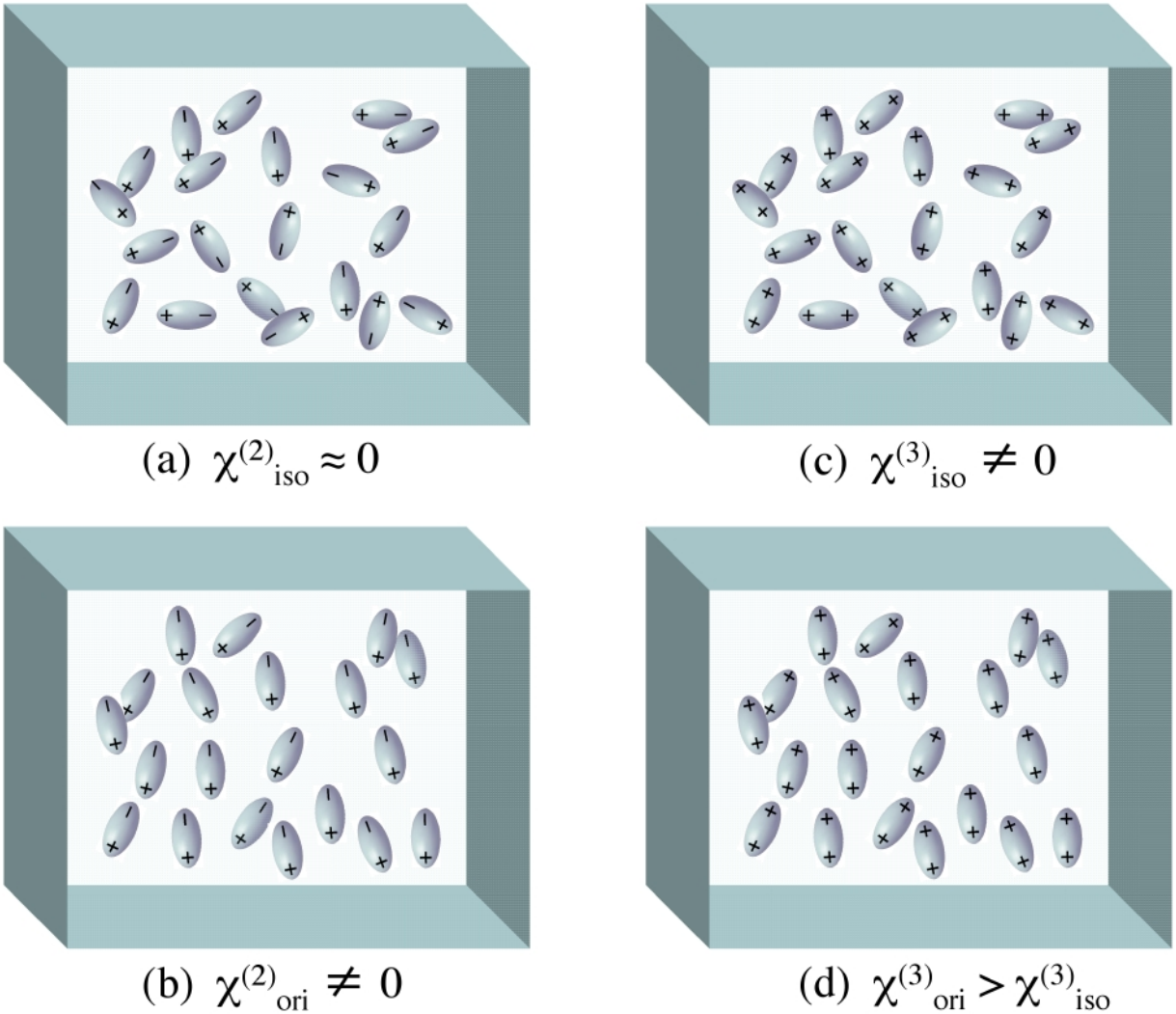

Figure 17.2 $\chi^{(2)}$ behavior for non-centrosymmetric molecules in an (a) isotropic state and in a (b) highly-ordered or oriented state. $\chi^{(3)}$ behavior for centrosymmetric molecules in an (c) isotropic state and in an (d) oriented state.

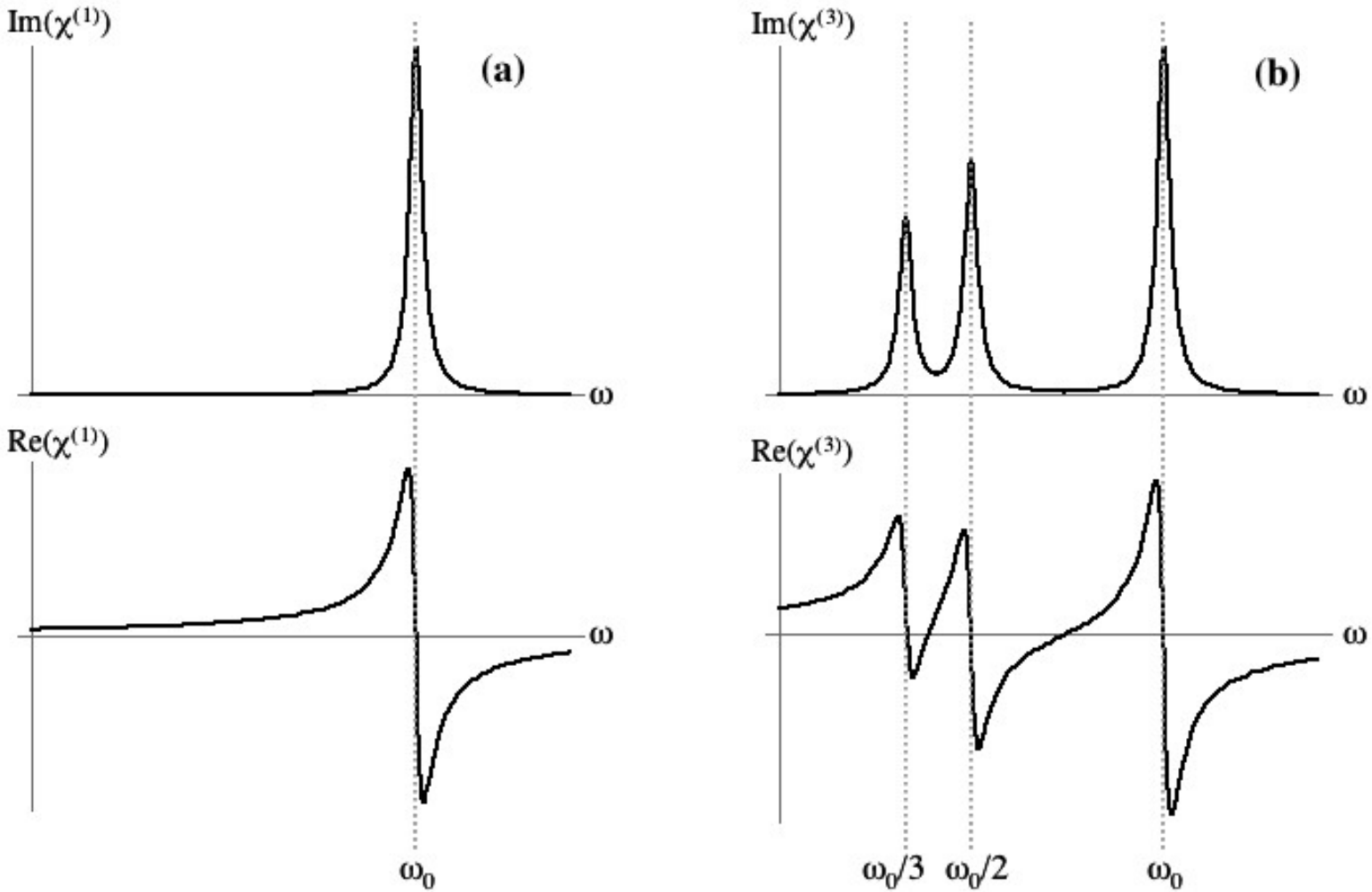

Figure 17.3 Typical dispersion for (a) $\chi^{(1)}$ and (b) $\chi^{(3)}$ in a medium with a single electronic resonance at ω_0. The upper plots show the imaginary parts of the susceptibility and the lower plots show the real part.

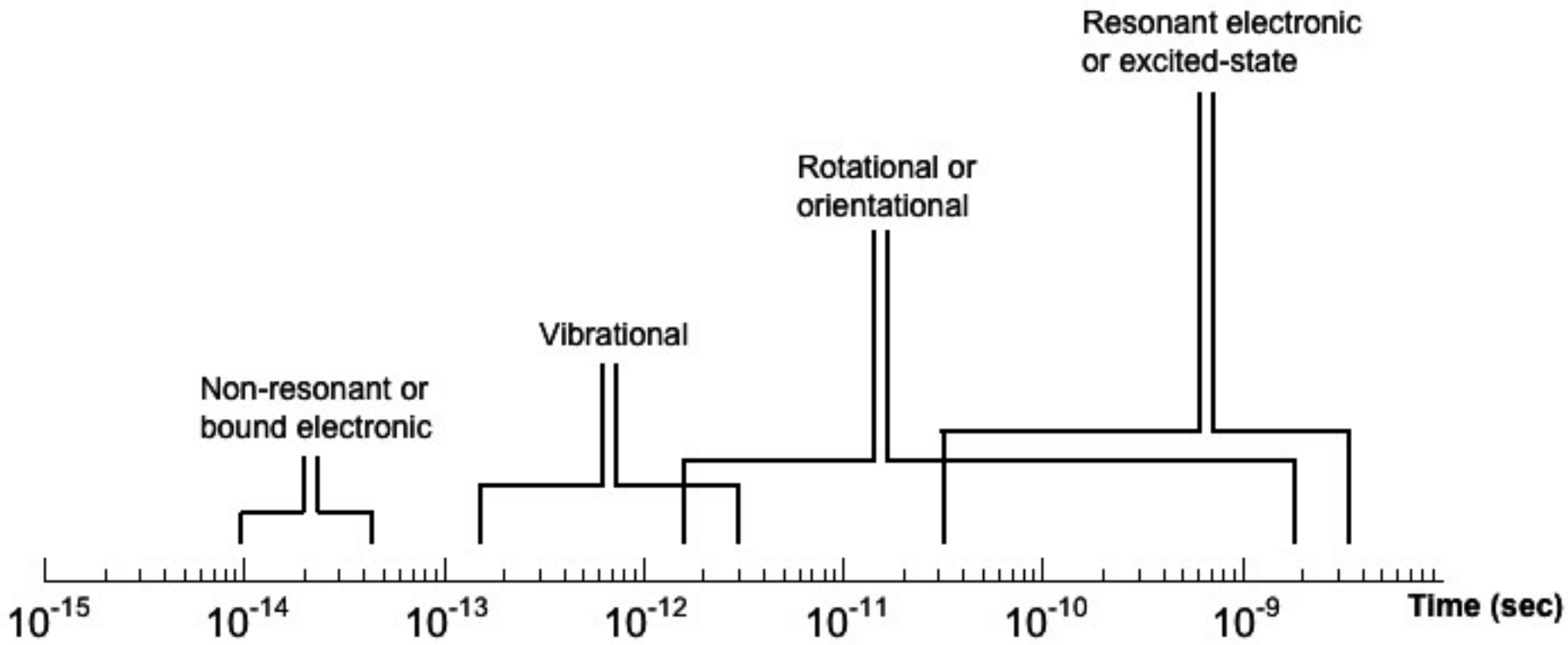

Figure 17.4 Typical temporal responses for various mechanisms of the third order nonlinear polarization in molecular systems.

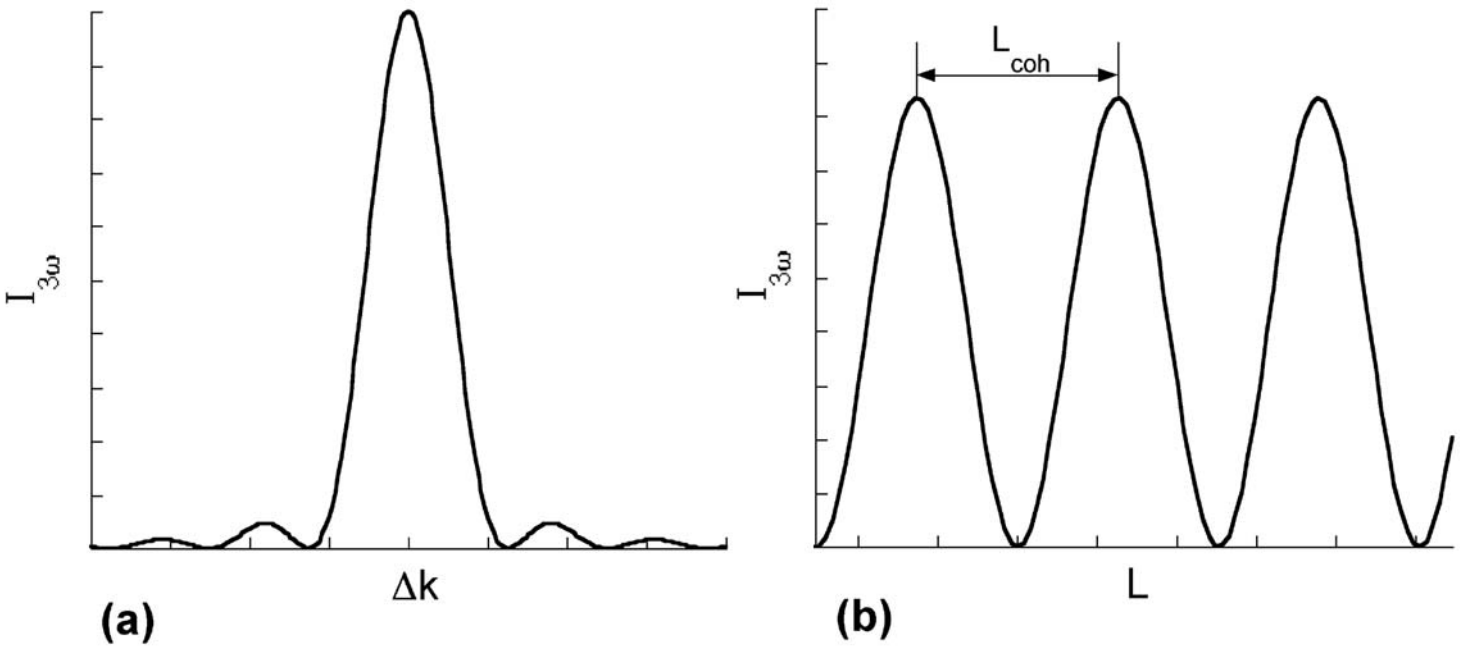

Figure 17.5 Third-harmonic signal intensity plotted versus (a) wave-vector or phase mismatch Δk for a constant thickness and versus (b) thickness L for a constant wave-vector mismatch. L_{coh} denotes the coherence length in the THG fringe pattern.

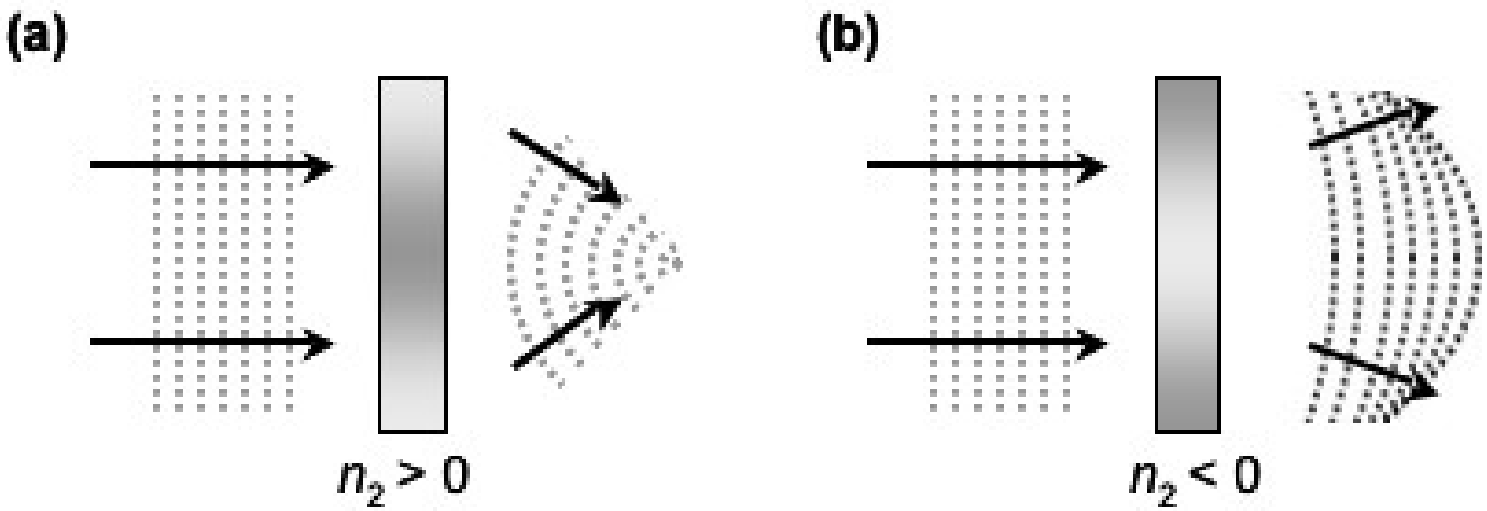

Figure 17.6 The effects of a spatially non-uniform induced phase change (illustrated in the samples) on incident phase fronts. (a) D epicts self-focusing in a medium with a positive n_2 or $\chi^{(3)}$ and (b) depicts self-defocusing in a medium with a negative n_2 or $\chi^{(3)}$. The arrows denote the direction of energy flow.

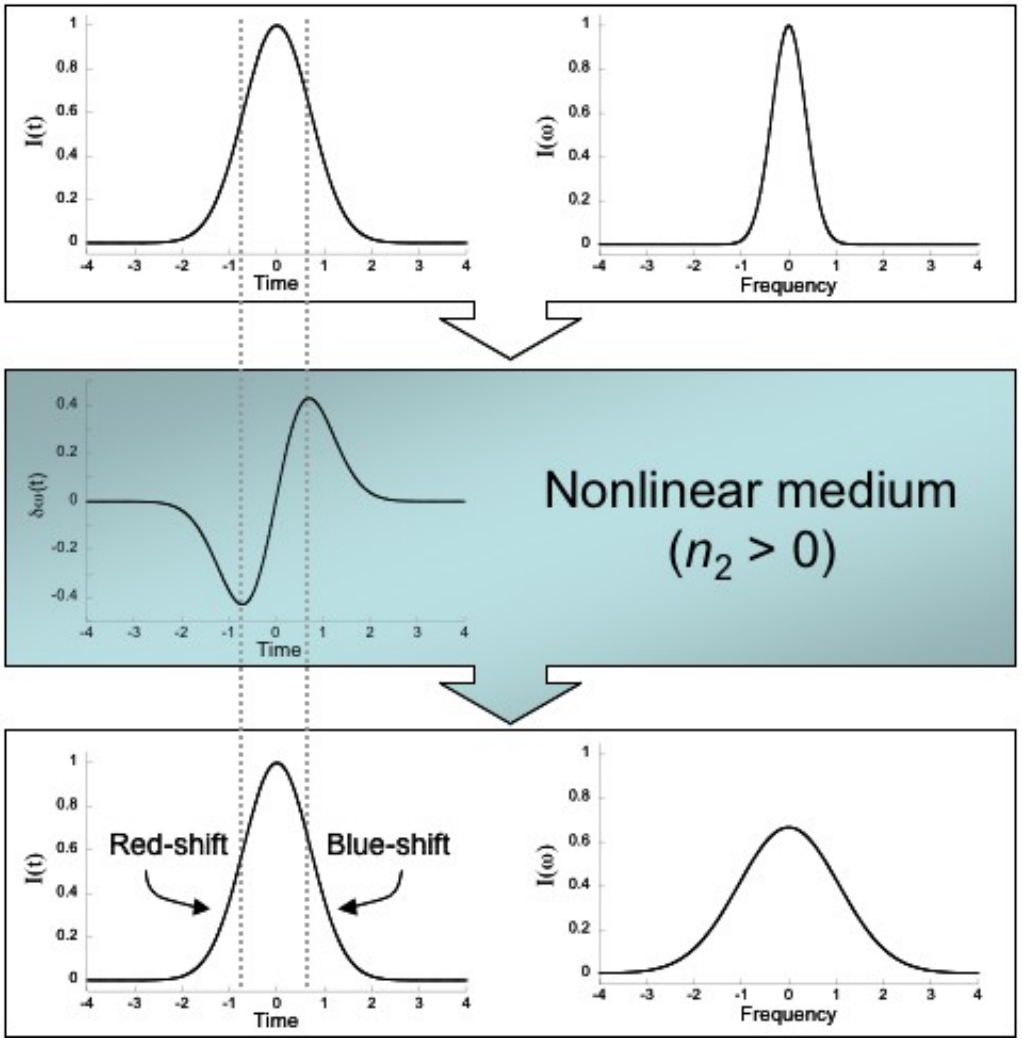

Figure 17.7 The effects of self-phase modulation on a pulse passing through a medium with a positive n_2 or $\chi^{(3)}$. The temporal pulse profile and frequency spectrum prior to entering the medium (top), the SPM-induced frequency shift in the medium (middle), and the pulse profile and spectrum after exiting the medium (bottom).

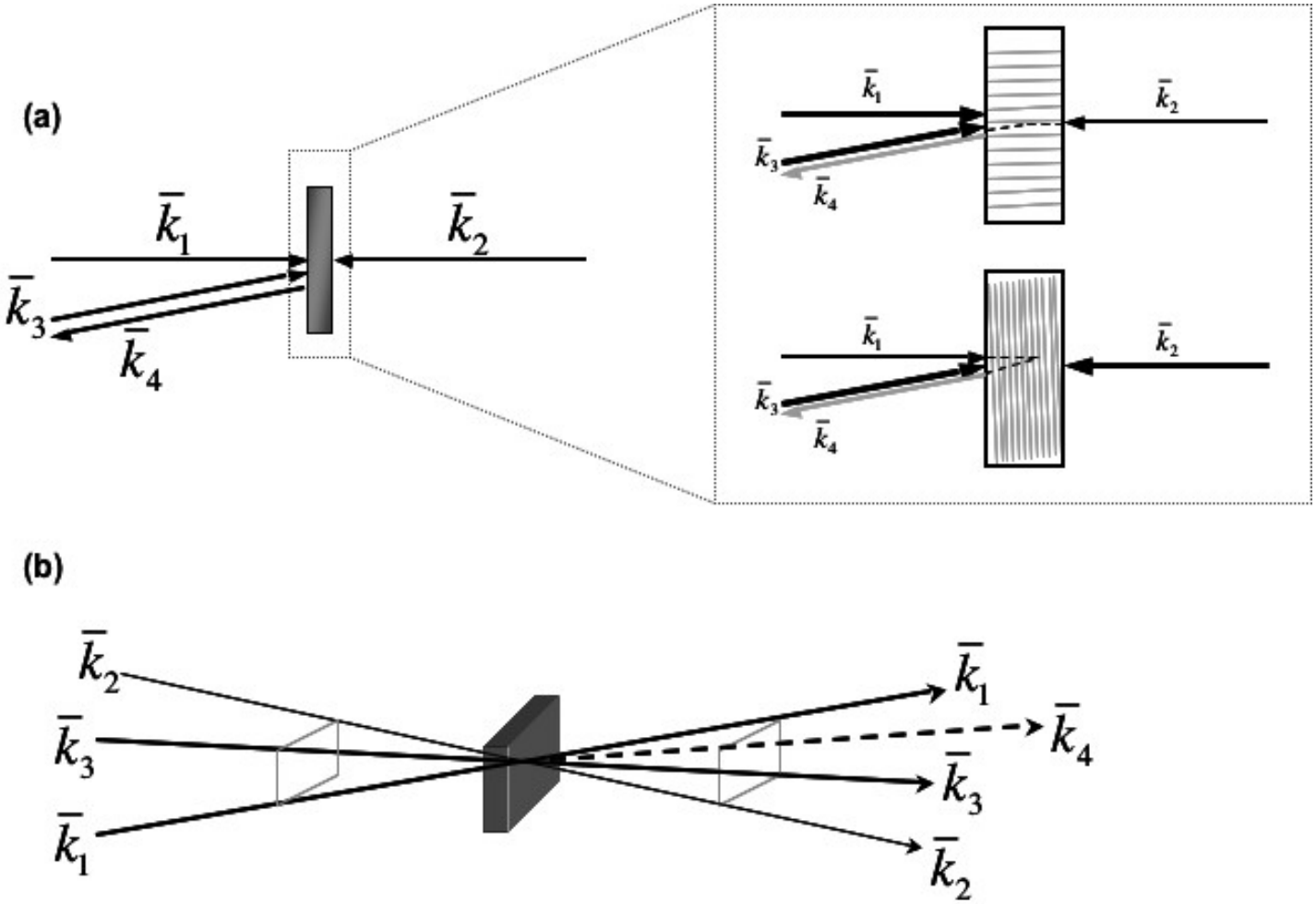

Figure 17.8 Typical geometries for DFWM: (a) counter-propagating or backward geometry and (b) folded-boxcars or forward scattering geometry. Inset to (a) shows the laser-induced gratings produced in the backward DFWM geometry as described in the text.

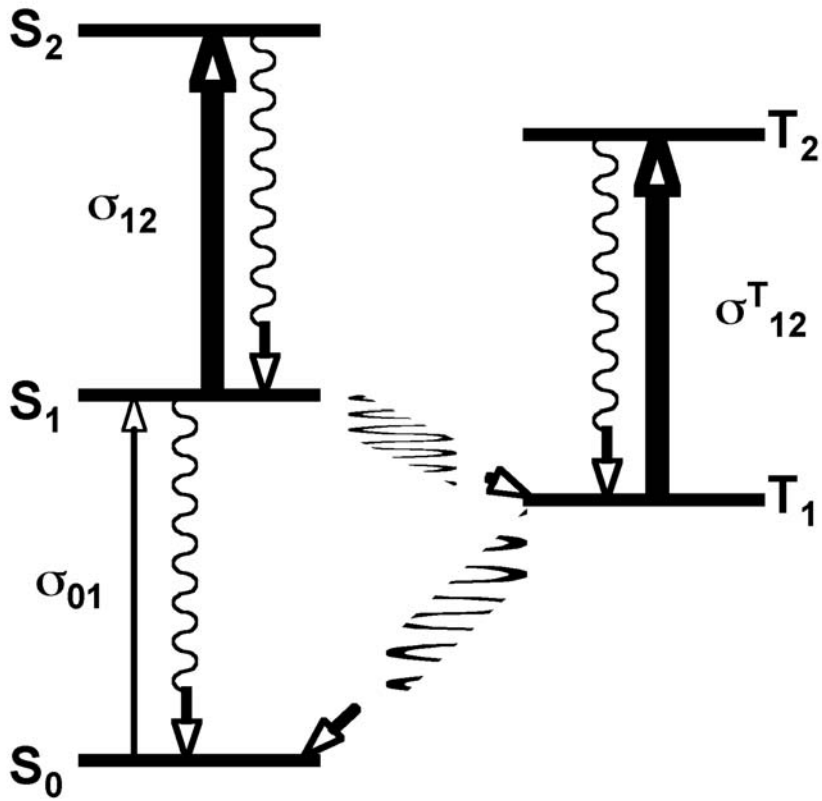

Figure 17.9 Five-level state diagram typically used to illustrate the transitions involved in reverse saturable absorption. Singlet and triplet excited-state absorption are denoted by bold arrows.

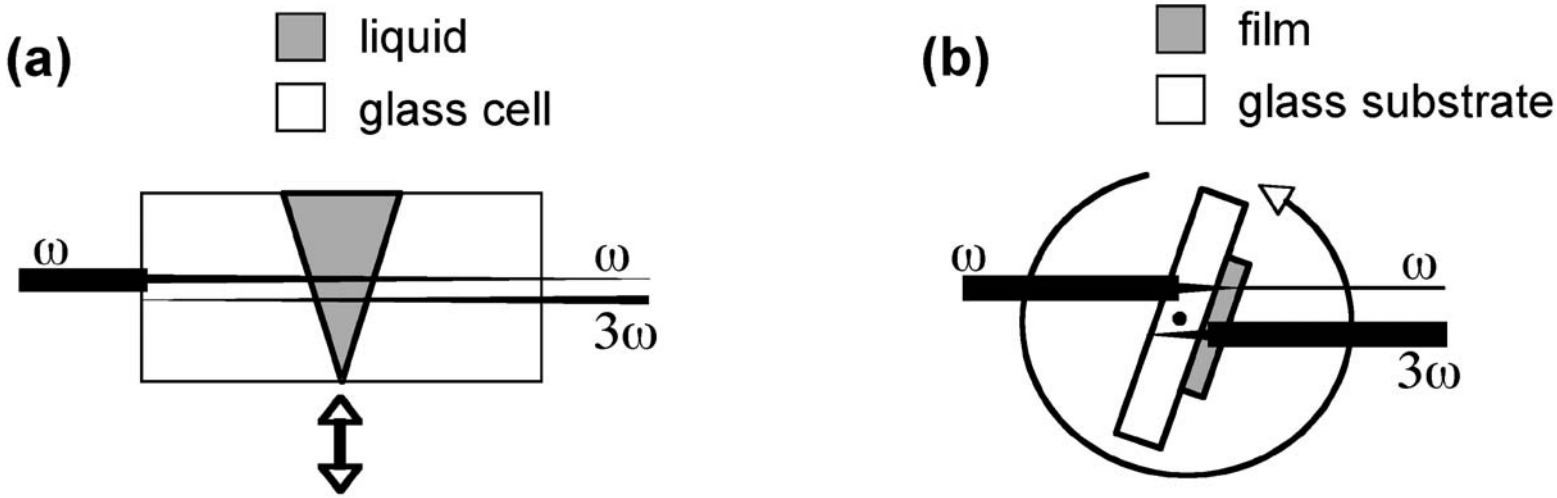

Figure 17.10 Typical experimental geometries for the use of THG as a nonlinear characterization technique. Figure (a) ill ustrates the wedge ge ometry fringe technique and Figure (b) shows the slab geometry Maker fringe technique.

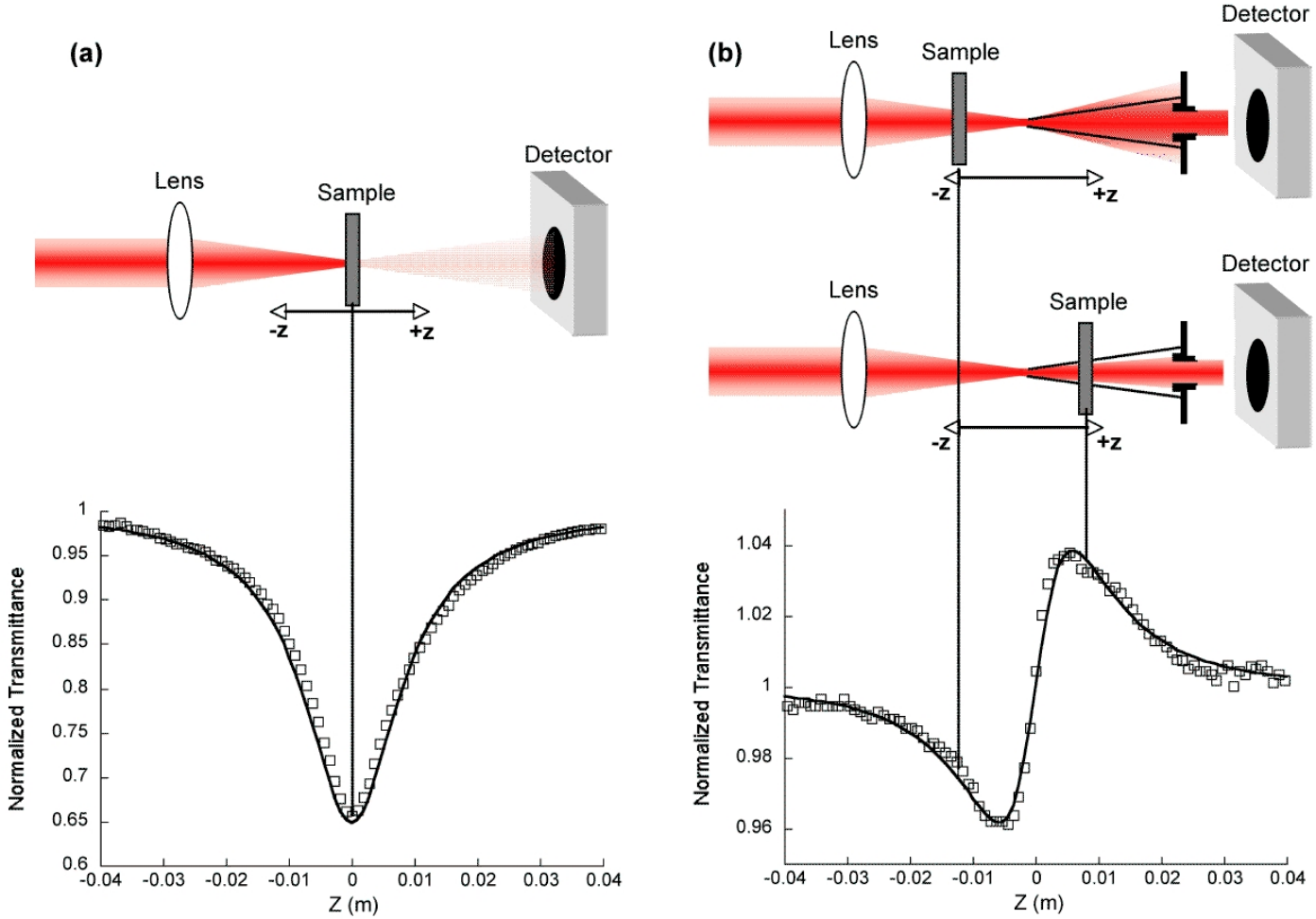

Figure 17.11 Optical layouts (top) and typical experimental data performed at 1.3 μm (bottom) for the Z-scan technique. (a) Open-aperture Z-scan data for a 410 μm slab of gallium arsenide. (b) Closed-aperture Z-scan data for a 1 mm slab of fused silica. Open squares represent experimental data points and solid lines are curve fittings performed according to Reference 21.

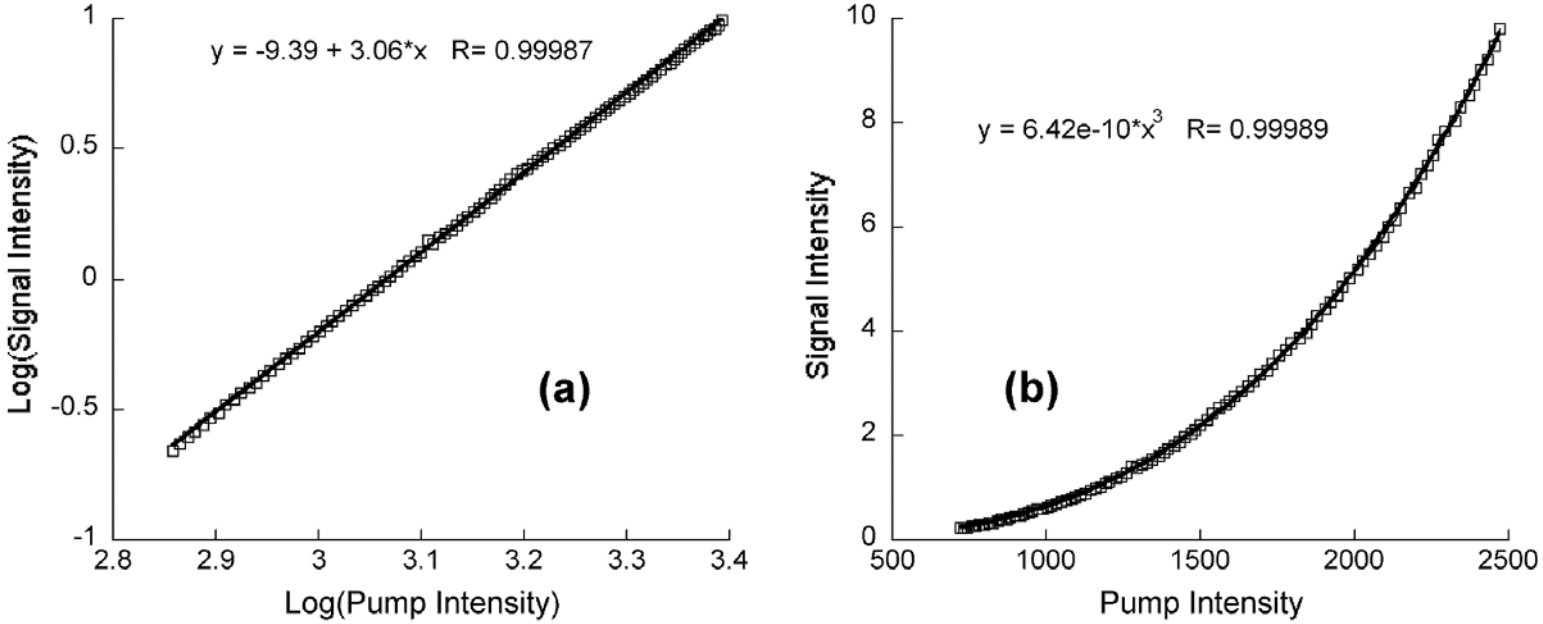

Figure 17.12 Experimental data from the power-dependent DFWM technique for a 500 μm slab of fused silica measured at 1.3 μm. Figure (a) shows the log-log plot of the power-dependent data given in Figure (b). Open squares represent experimental data points and solid lines are curve fittings revealing the cubic dependence of the nonlinearity.

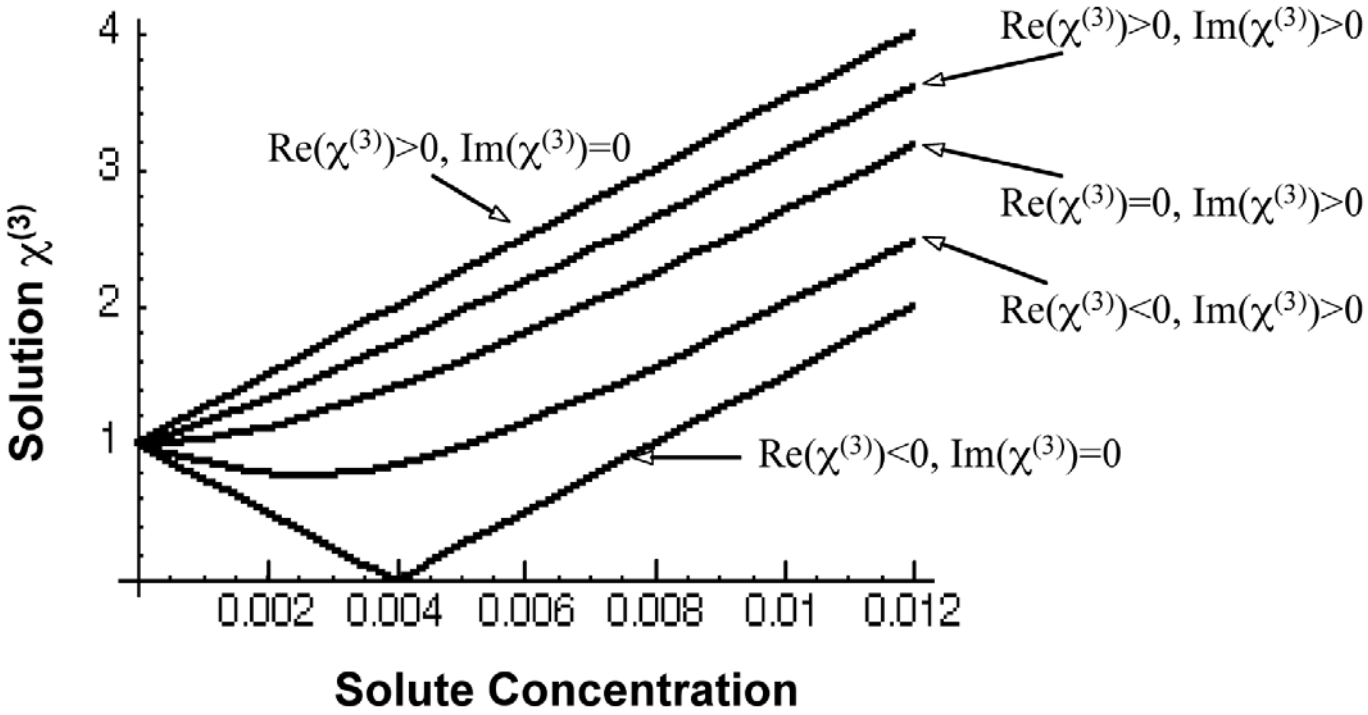

Figure 17.13 Graphical representation of the concentration dependence of $\chi^{(3)}$ for a solution as measured by the DFWM technique. The solvent is assumed to have a positive $\mathrm{Re}(\chi^{(3)})$ and the particular constitution of the solute $\chi^{(3)}$ is described by each plot label.

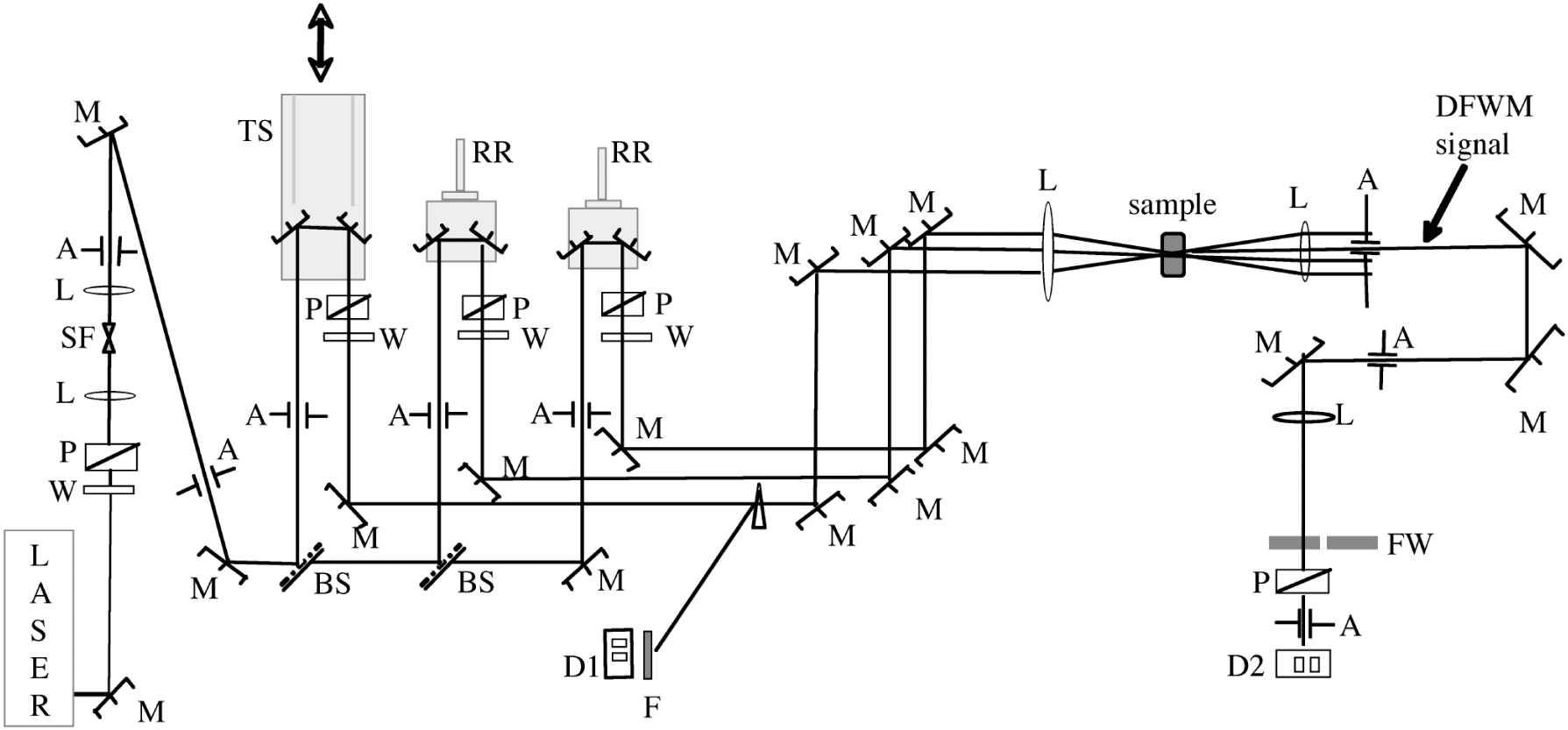

Figure 17.14 Typical optical layout for a forward-scattering DFWM experiment: D1,D2 Š detectors, W Š waveplate, P Š polarizer, A Š aperture, L Š lens, F Š filter, FW Š filter wheel, M Š mirror, BS Š beamsplitter, TS Š translation stage, RR - retroreflector, SF Š spatial filter.

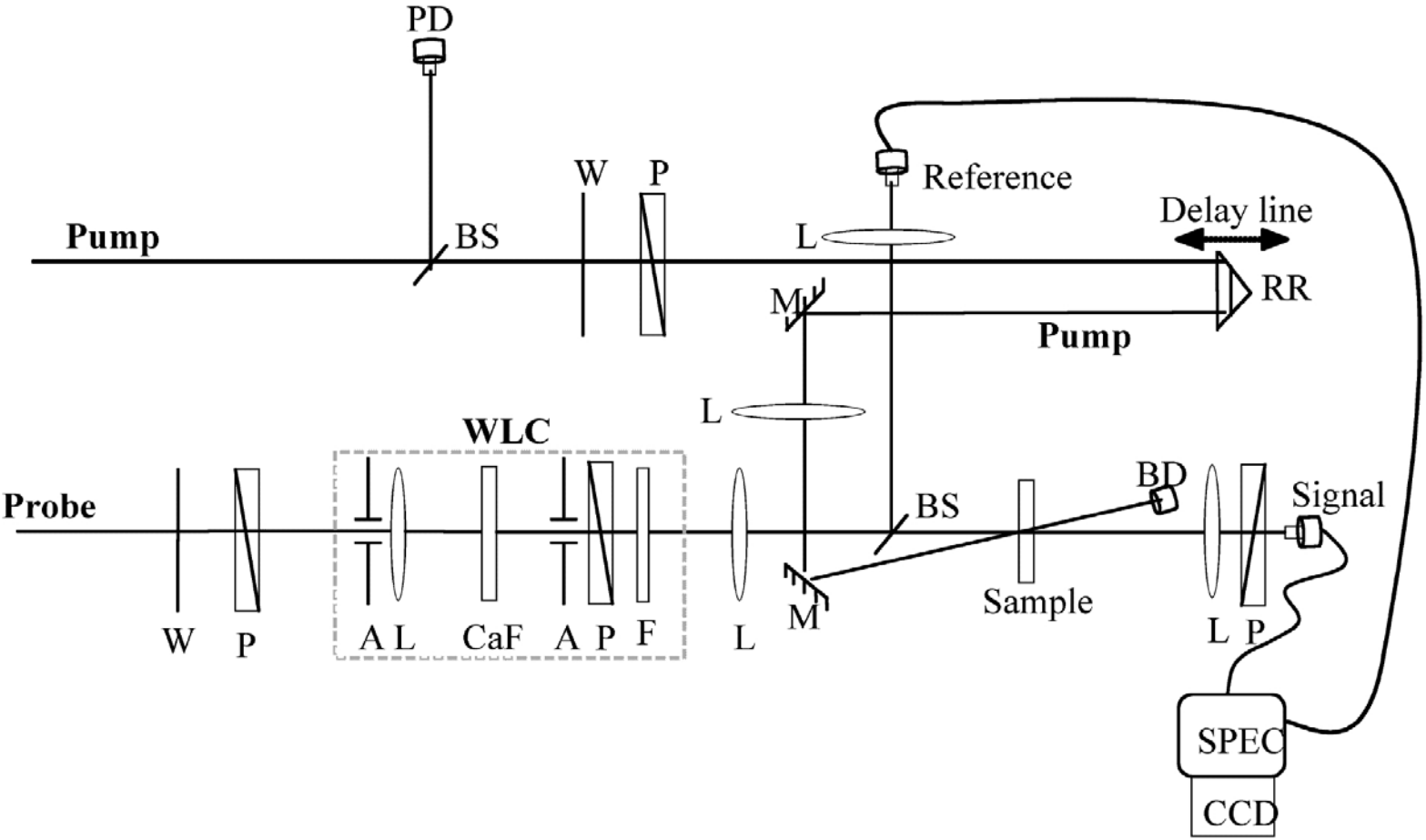

Figure 17.15 Typical optical layout for a pump-probe experiment [29]: PD Š photodiode, W Š waveplate, P Š polarizer, A Š aperture, L Š lens, F Š filter, CaF Š calcium fluoride window, M Š mirror, BS Š beamsplitter, RR Šretroreflector, BD Š beam dump, SPEC Š dual fiber input spectrometer, CCD Š dual Charge Couple Device array. Optional generation of WLC probe is shown inside the dashed box.

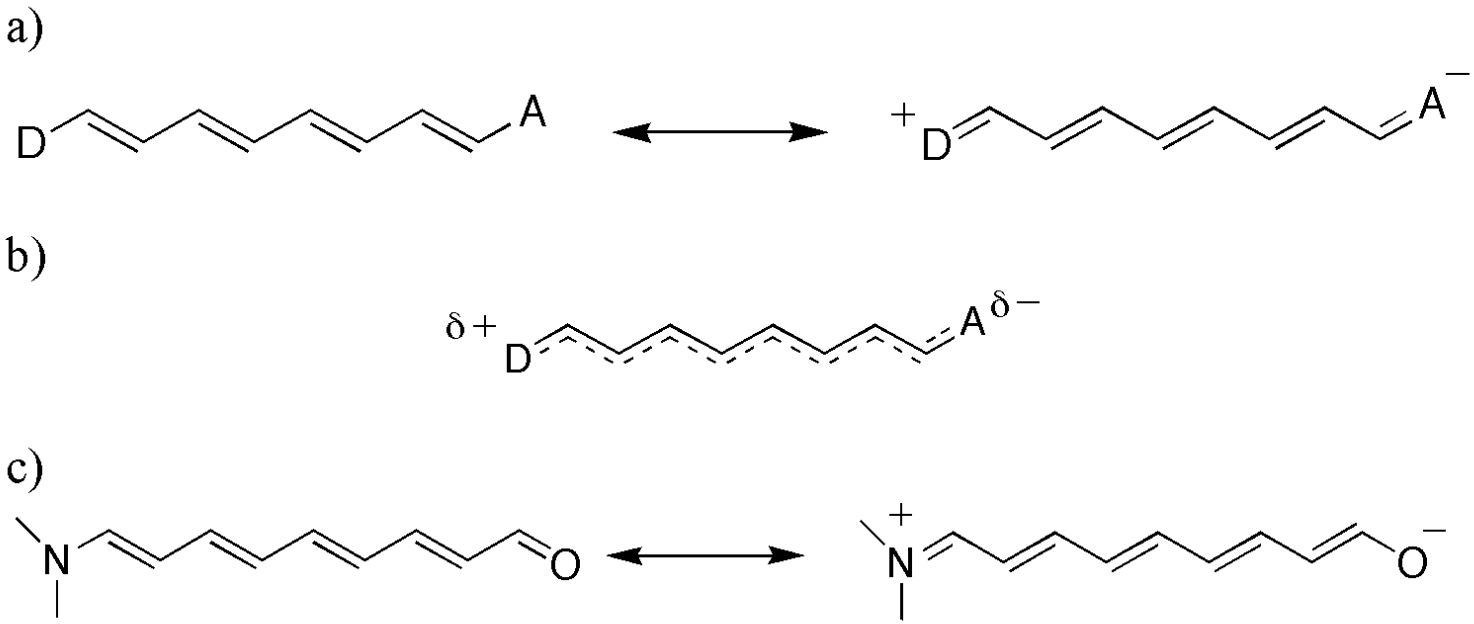

Figure 17.16 a) Neutral (left) and charge transfer (right) resonance structures for a donor-acceptor polyene. b) Delocalized structure resulting from superposition of the two resonance structures. c) Resonance structures for $(CH_3)_2N\text{-}(CH{=}CH)_4\text{-}CHO$.

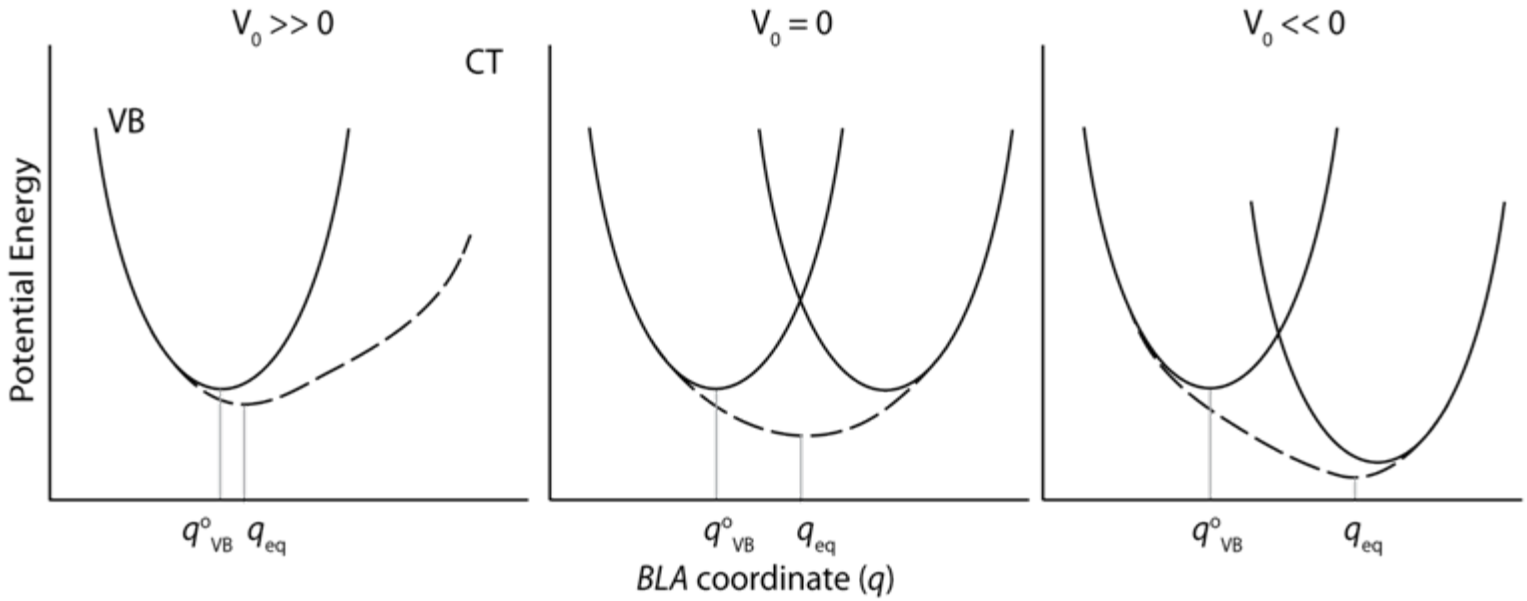

Figure 17.17 Illustration of ground state potential surfaces (dashed line) for different relative energies of VB (solid, left) and CT (solid, right) states showing the changes of the equilibrium structure due to the mixing of the VB and CT states. The light vertical lines indicate the equilibrium coordinates for the VB (q^{o}_{VB}) and ground state (q_{eq}).

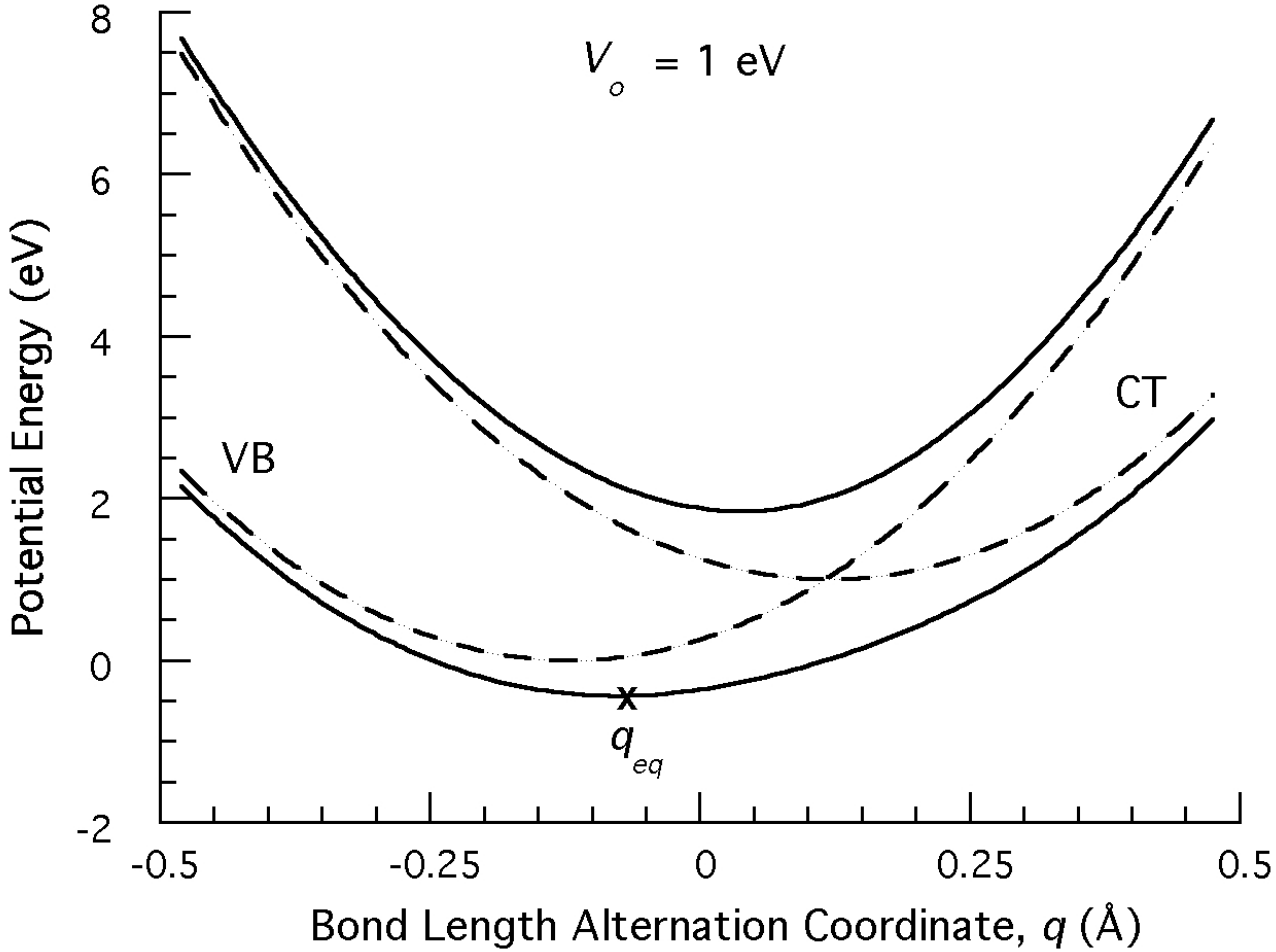

Figure 17.18 Calculated potential energy surfaces for the ground and excited state (solid lines) resulting from the mixing of valence bond (dashed, left) and charge transfer (dashed right) potential surfaces. The parameters used were: V_0 = 1 eV, t = 1.1 eV and k = 33.55 eV/Å^2. The equilibrium coordinates for VB and CT are -0.12 Å and 0.12 Å, respectively. The x marks the equilibrium coordinate (q_{eq}) on the ground state potential surface.

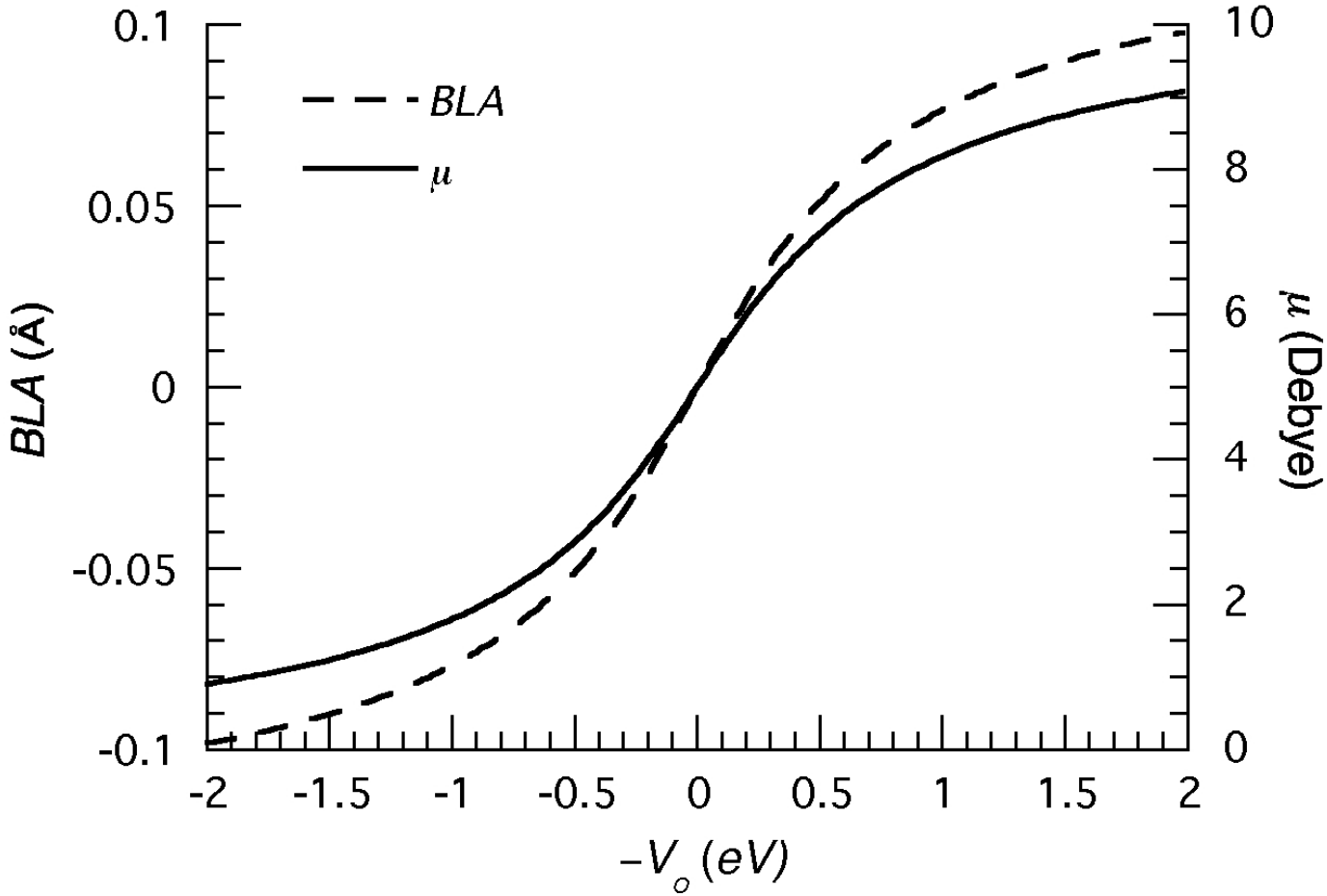

Figure 17.19 Bond length alternation and ground state dipole moment as $-V_0$ is varied from -2 to 2 eV calculated using the VB-CT model, for the case of t = 1.1 eV and k = 33.55 eV/Å^2. These values have been plotted against $-V_0$ in order to have the sense of going from the VB form dominating on the left to having the CT form dominating on the right.

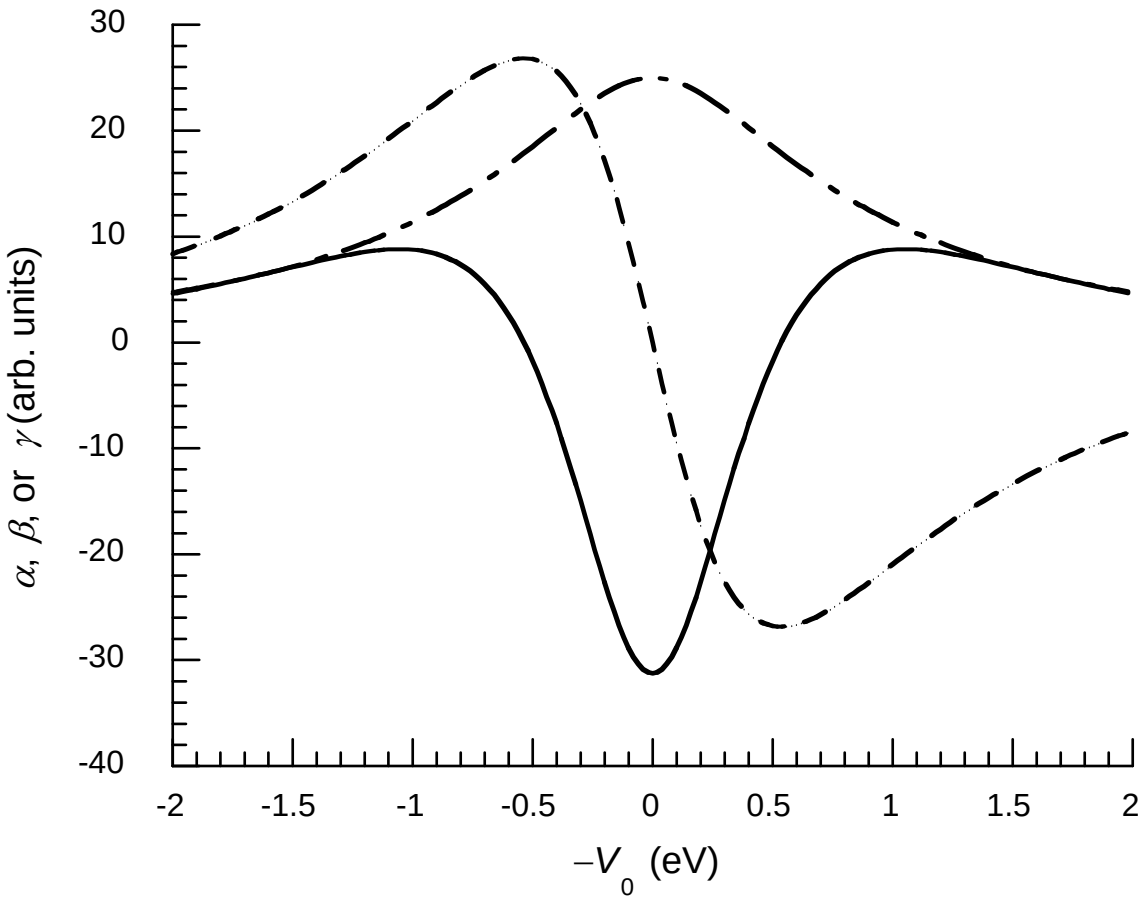

Figure 17.20 Trends of α (dash-dot line), β (dashed line), and γ (solid line) as a function of $-V_o$ calculated using the VB-CT model for the model DA molecule $(CH_3)_2N\text{-}(CH{=}CH)_4\text{-}CHO$. The VB form dominates at the left and the CT form dominates at the right of the plot.

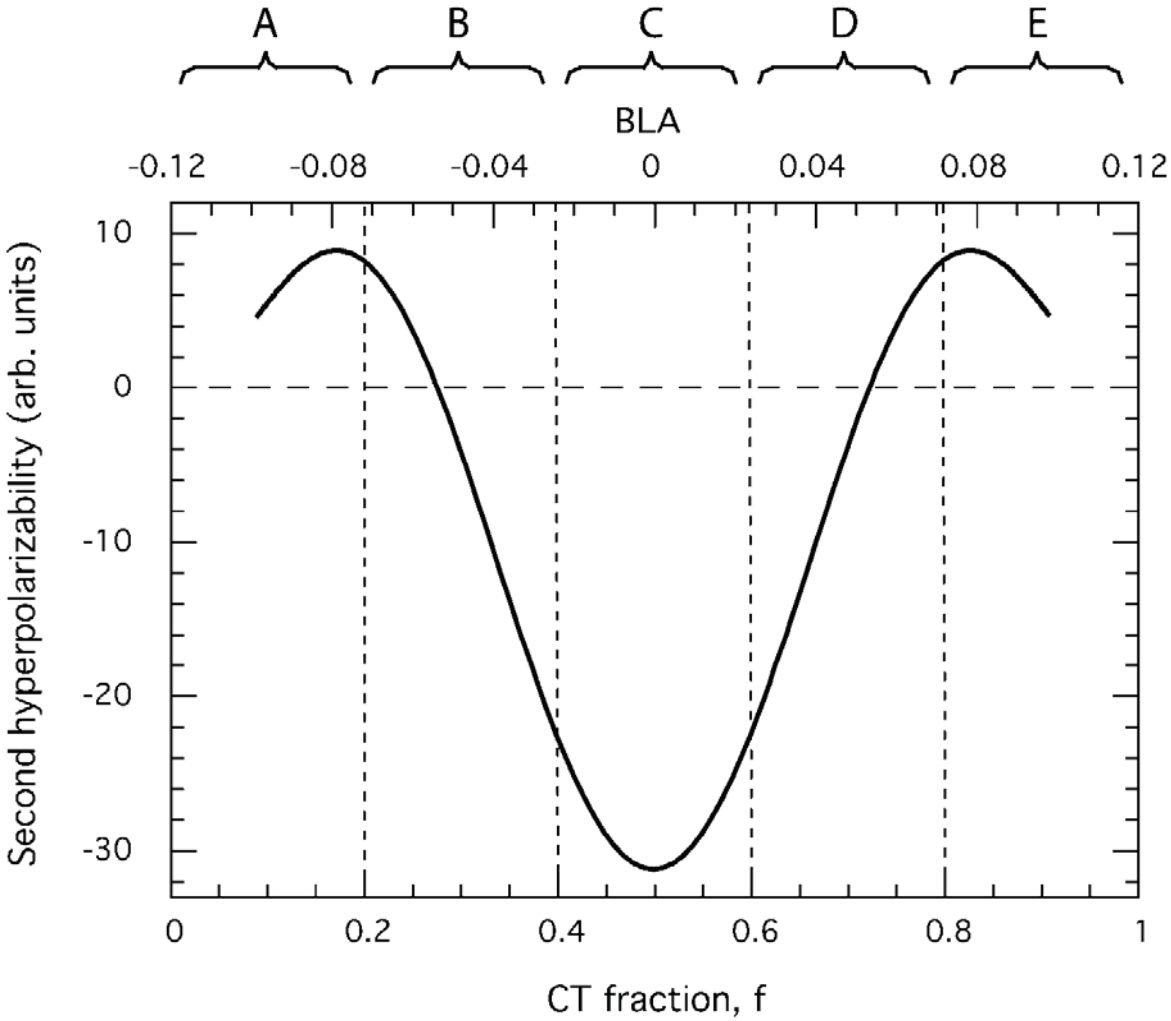

Figure 17.21 Second hyperpolarizability from Figure 20 plotted as a function of the charge transfer fraction, *f*, and the bond length alternation parameter, *BLA*. The range of *f* and *BLA* has been broken up into 5 regions, A-E, to qualitatively group molecules of similar behavior.

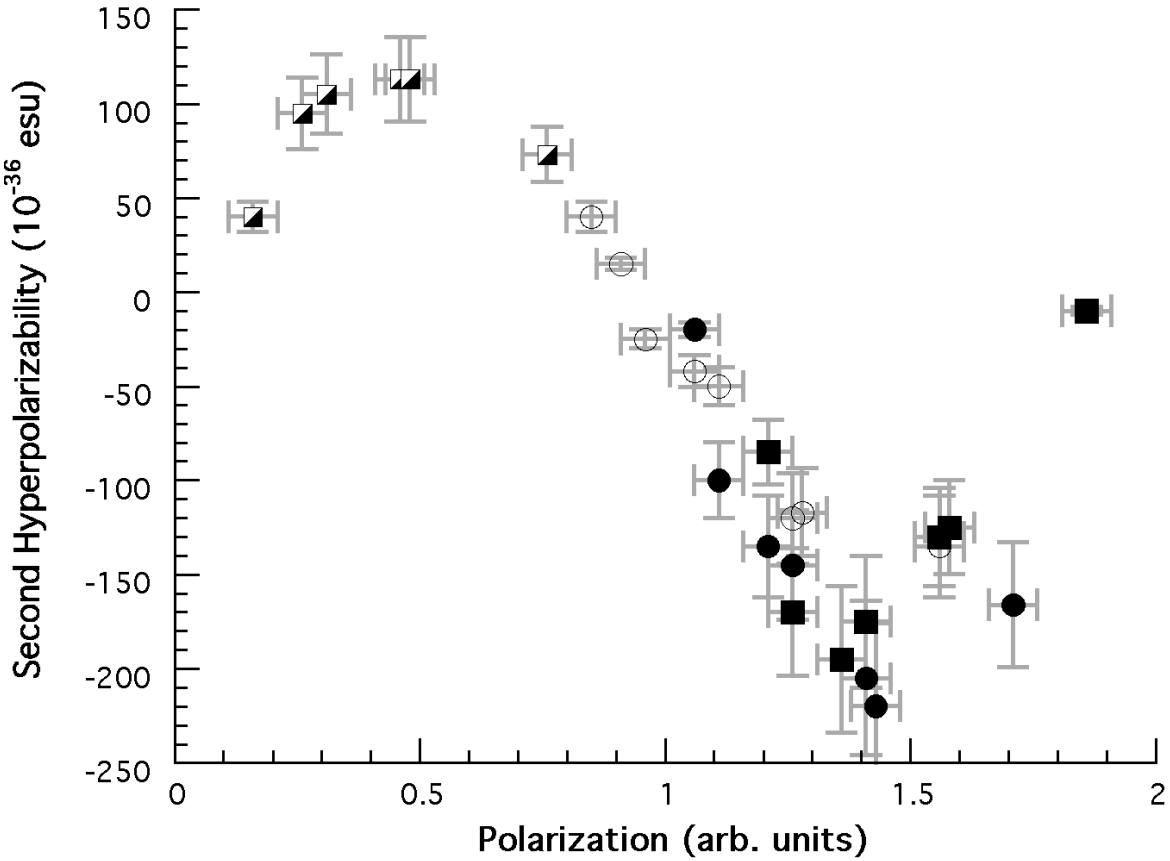

Figure 17.22 Second hyperpolarizability of donorŠacceptor triene molecules listed in Table 3 plotted versus a measure of the polarization of the molecules based on the solvent $E_T(30)$ parameter. The data from Table 3 were spliced together by adding an amount to the $E_T(30)$ parameter to approximately match the hyperpolarizability values. The data points correspond to the molecules with the following acceptors: aldehyde (split square), dicyano (open circle), barbituric acid (filled circle), and thiobarbituric acid (filled square).

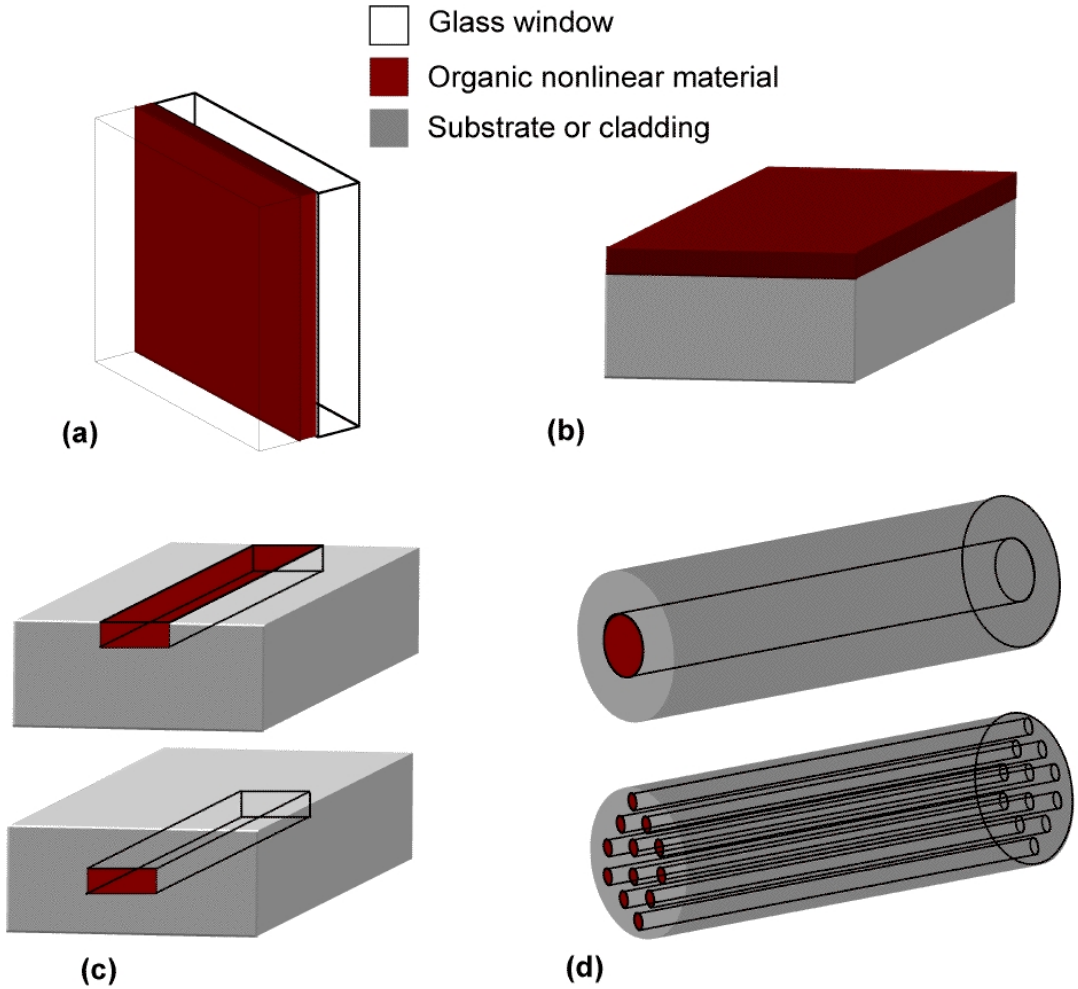

Figure 17.23 Architectures typically employed for integrating organic nonlinear materials into devices. (a) L arge area b ulk nonlinear material enclosed between glass windows. (b) Slab waveguide for one-dimensional confinement of light. (c) Channel waveguides (surface Š top, buried Š bottom) for two-dimensional confinement of light. (d) Microstructure fiber waveguides for two-dimensional confinement of light.

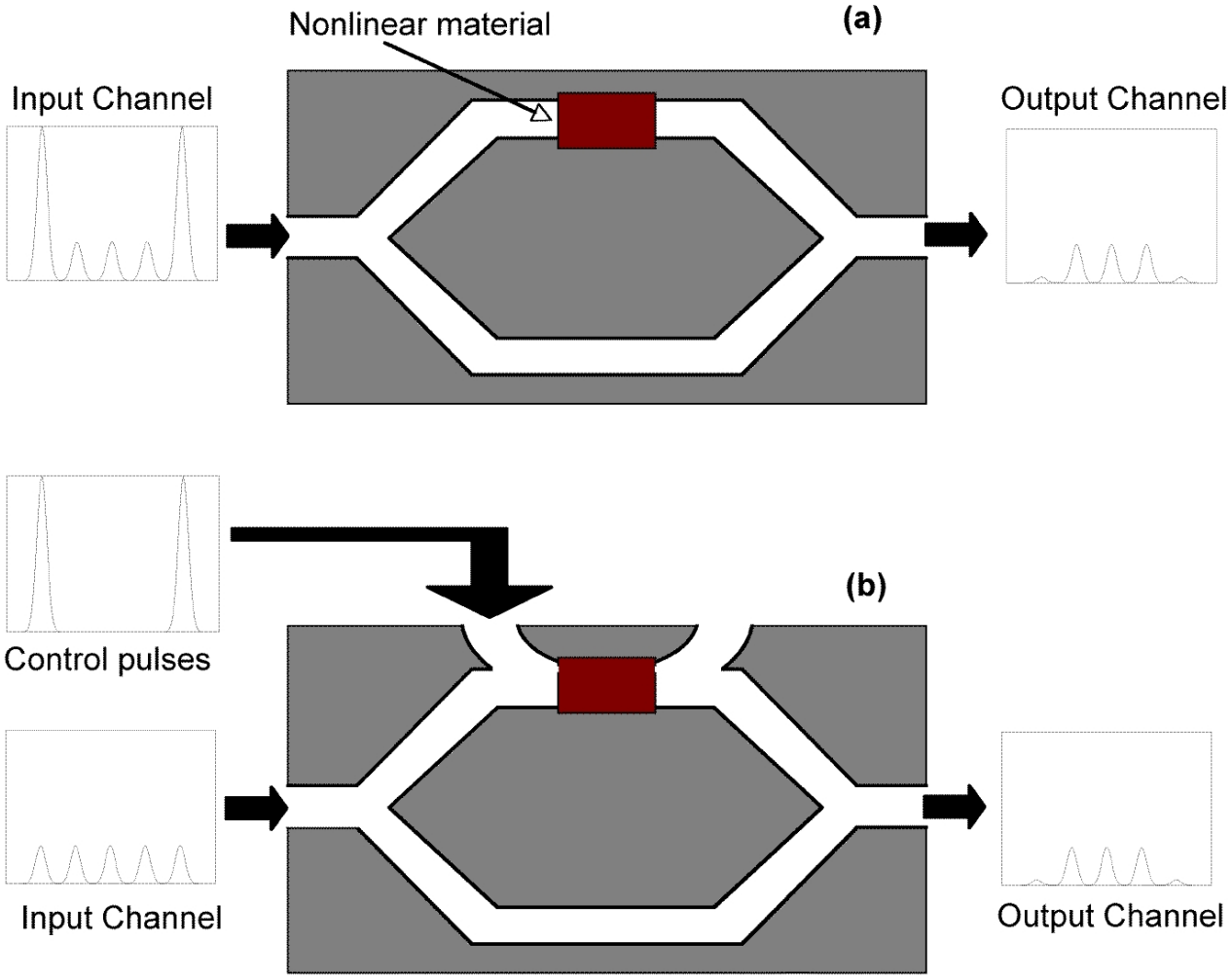

Figure 17.24 Illustration of temporal demultiplexing via all-optical switching in a nonlinear Mach-Zehnder interferometer. (a) Switching using self-phase modulation. (b) Switching using cross-phase modulation.

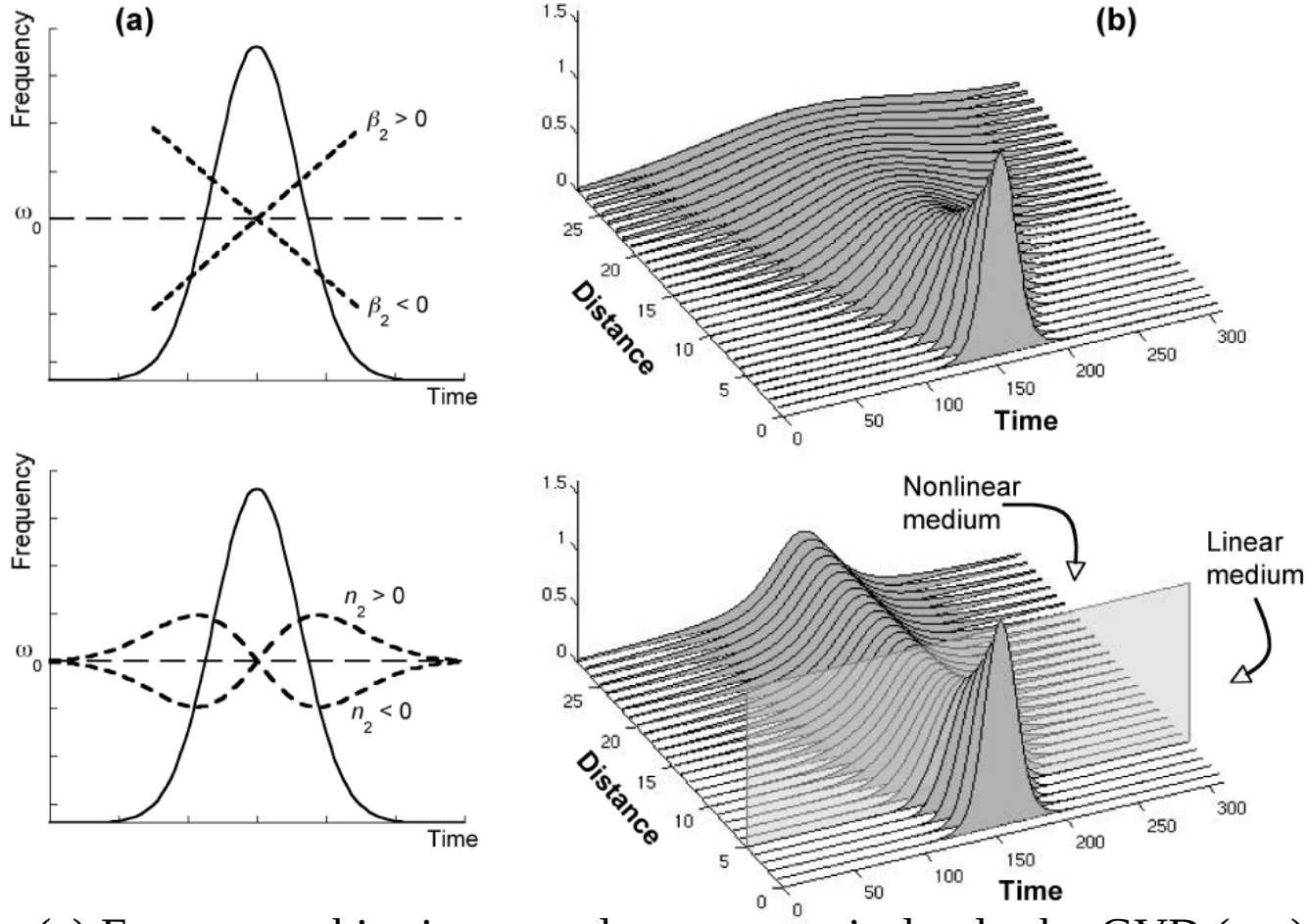

Figure 17.25 (a) Frequency chirp impressed upon an optical pulse by GVD (top) and by SPM (bottom). (b) Simulation of pulse broadening (top) during propagation through a linear medium exhibiting GVD ($\beta_2 < 0$) a nd the formation of a t emporal soliton (bottom) after compensation of the frequency chirp from GVD ($\beta_2 < 0$) by the frequency chirp from SPM ($n_2 > 0$). The vertical plane (in bottom graph) denotes a separation between a purely linear medium (as in the top graph) and a medium exhibiting both linear and nonlinear characteristics.

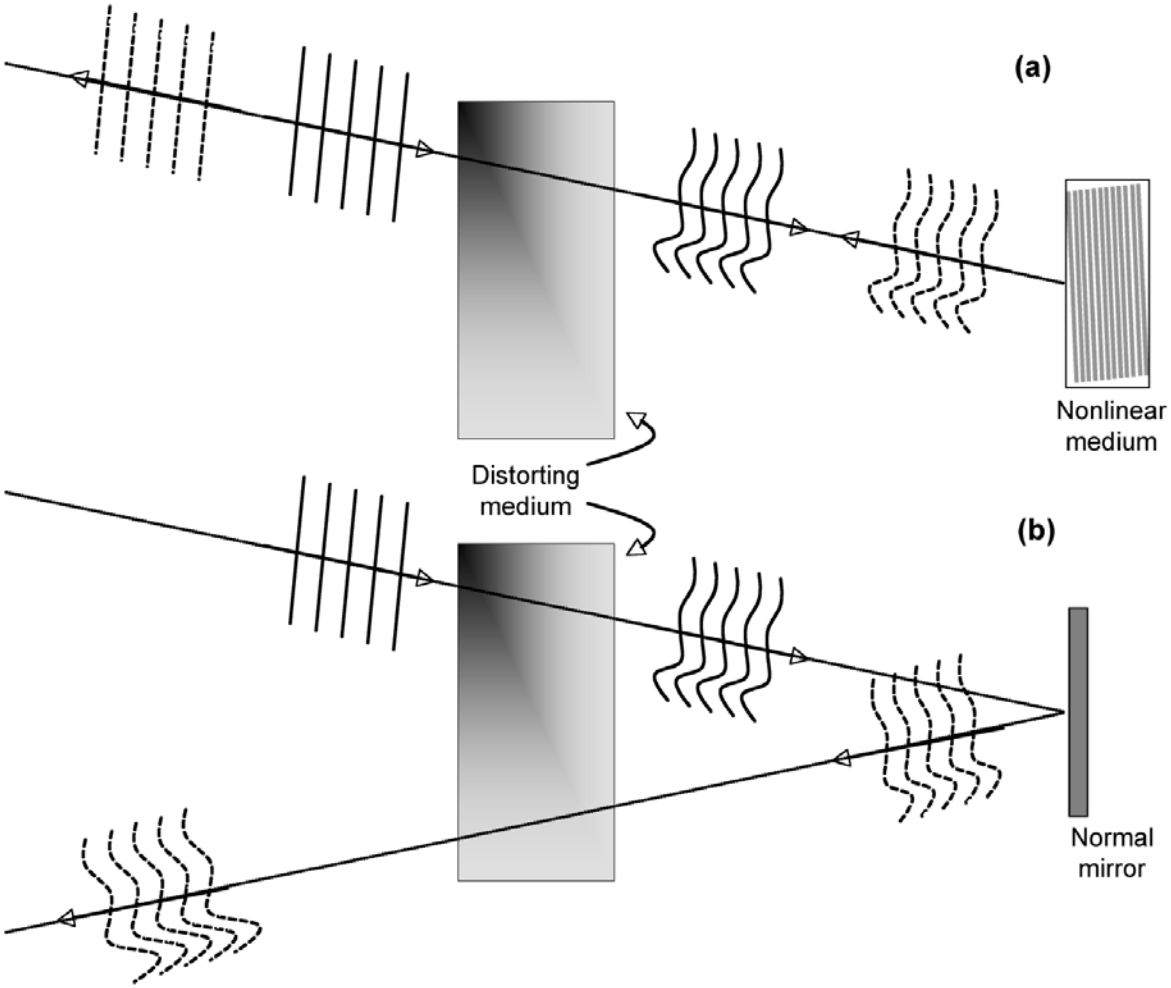

Figure 17.26 Potential scenarios for optical wave fronts following passage through a distorting medium. (a) Wave front aberration correction as a consequence of nonlinear OPC. (b) Further wave front deterioration due to reflection off a normal mirror. Solid lines Š incoming wavefronts, dashed lines Š outgoing wavefronts.

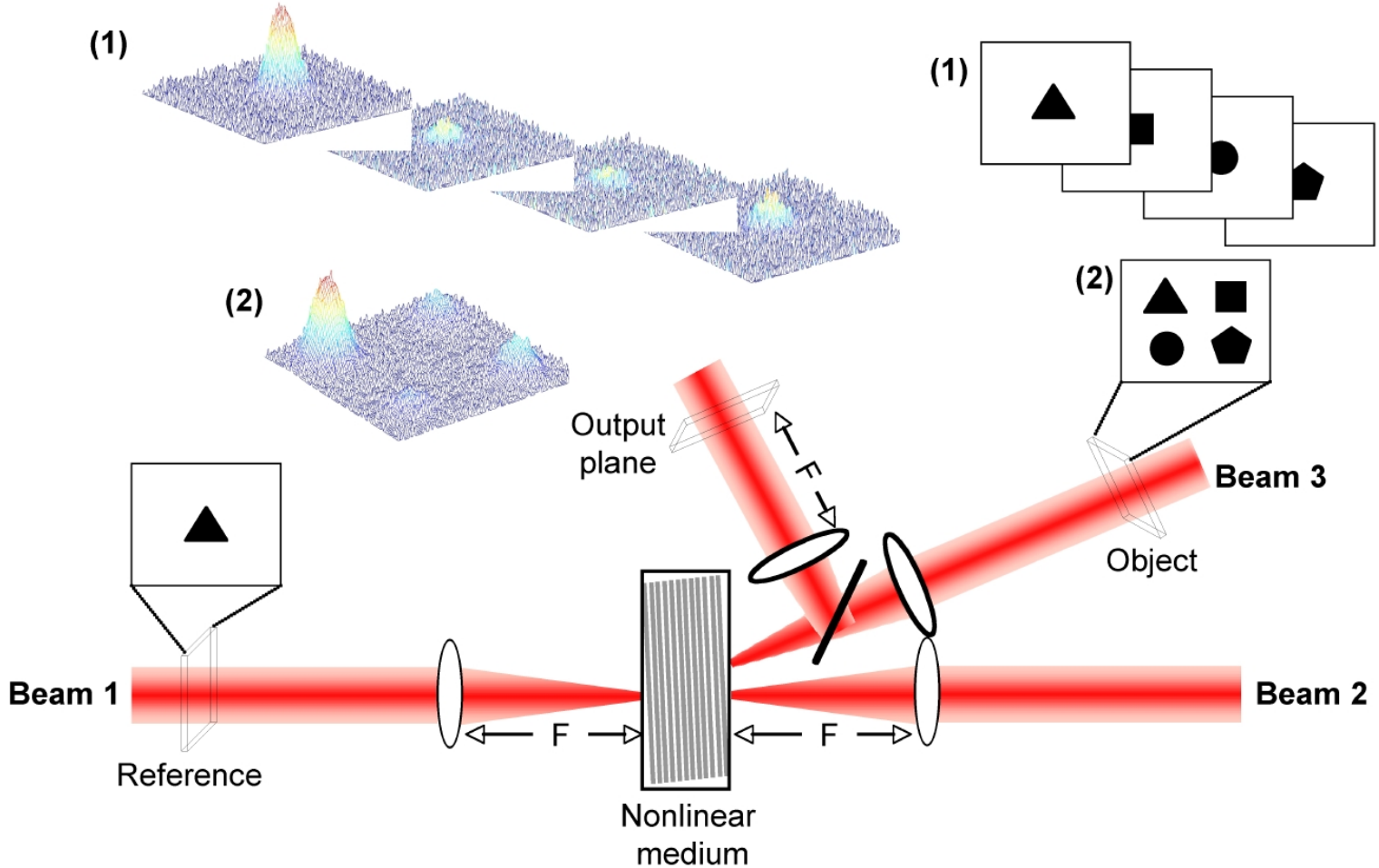

Figure 17.27 Typical phase conjugate geometry employed for real-time image recognition. Since beam 2 possesses no spatial information, the output plane represents a simple cross-correlation between the reference image (beam 1) and the object image (beam 3). Case 1 represents identification of the reference image from a series of single-element object images while case 2 demonstrates identification from a multi-element object image.